Experimental Study of the Surface Waves on a Dielectric Cylinder via Terahertz Impulse Radar Ranging

Roger W. McGowan, R. Alan Cheville, and Daniel R. Grischkowsky, *Fellow, IEEE*

***Abstract*—Employing an ultrafast optoelectronic terahertz impulse radar range with subpicosecond resolution, we have characterized the electric-field time-domain response from an impulsively excited dielectric cylinder. The bandwidth of the measurement extends from 200 GHz to 1.4 THz and late time response is observed at times exceeding that to traverse 40 target radii at c. A physical optics (PO) model is employed to identify the different mechanisms of scattering for the temporally isolated signals. Through analysis of the first and second surface-wave signals it is determined that the surface wave has a propagation velocity of $0.91c$ and an effective index of refraction of $n = 1.10 + 0.073i$. The first measurement of the coupling efficiency of this surface wave through the cylinder via an interior chord at the critical angle is performed along with the determination of the $\pi/2$ phase shift associated with the single axis caustic of this interior chord in the PO model.**

***Index Terms*—Electromagnetic scattering, inverse problems, time-domain measurements.**

I. Introduction

THE interest in scattering experiments on conducting and dielectric bodies is wide reaching and many early theoretical works have dealt with the scattering of electromagnetic (EM) waves from spheres and other simple models such as cylinders. This study has primarily been done in the frequency domain. More recently, there has been a renewed interest in the scattering from dielectric targets particularly due to the advent of the short pulsed laser and its applications in areas such as weather measurements and lidar as well as basic research where a detailed understanding of the time-domain response is critical. Time-domain measurements can provide additional physical insight into the scattering mechanisms since they are distinguished by the time of arrival of their scattered pulses.

In this paper, we present a time-domain scattering measurement of a precise 3-mm-diameter alumina (aluminum–oxide) cylinder, which was taken on our terahertz impulse radar range [1], [2]. The measurement is compared to the calculated radar cross section (RCS) and the time-domain scattered signature. The fit between the experimental and theoretical RCS is excellent over a bandwidth from 200 GHz to 1.4 THz and the time-domain fit is also excellent over the entire 220-ps range of the data scan, which includes late time features as far out as $t = 40a/c$, where a is the cylinder radius and c is the speed of light in free space. From this precise, data the first- and second-order surface waves are independently analyzed using the physical optics (PO) model. The surface-wave propagation speed, effective index of refraction, coupling efficiency through the interior ray, and the associated single-axis caustic phase shift are determined. The exceptional accuracy of the data/theory comparison serves as a calibration of the terahertz time-domain impulse radar range, demonstrating the potential for applications to table-top ranging of scale model dioramas and scaled targets.

Manuscript received January 5, 1999; revised December 10, 1999. This work was supported in part by the National Science Foundation, and in part by the Army Research Office.

The authors are with the School of Electrical and Computer Engineering and the Center for Laser and Photonics Research, Oklahoma State University, Stillwater, OK 74078 USA.

Publisher Item Identifier S 0018-9480(00)02069-X.

II. Experiment and Theory

The impulse radar range, shown in Fig. 1(a), consists of an optoelectronic transmitter and receiver along with beam shaping and steering optics. A detailed description of the entire system has been previously published [1], [2]. In brief, 80-fs optical pulses at 820 nm from a KLM Ti:Sapphire laser are focused onto a coplanar stripline, which is dc biased at 70 V; an electron–hole plasma is optically generated and the subsequent acceleration of the carriers generates a near single cycle EM pulse of terahertz radiation. The beam of terahertz pulses is expanded and near planar wavefronts are attained at the far-field target 78 cm (2600 wavelengths at 1 THz) from the transmitter. At 1 THz, the deviation from planar phase fronts is only 0.005λ over the target diameter. The far-field scattered signal is collected at a bistatic angle of 13° and focused onto a 30-μm dipole antenna, which is photoconductively switched by a second beam of 80-fs pulses, which generates a dc current that is proportional to the instantaneous electric field of the scattered terahertz pulse. By scanning the relative delay between the detected pulse and gating optical pulse, the entire time-dependent scattered pulse is obtained, including both field and phase information.

The target for the study is a 3.001 ± 0.001-mm-diameter fine ground alumina cylinder with the low-frequency real part of the index of refraction $n_a = 3.17$. The system is first characterized by placing a reference, i.e., 30-mm-diameter copper cylinder at the target position; the reference cylinder has a spectrally flat response and yields an accurate measurement of the incident pulse, as shown in Fig. 1(b). Utilizing the cylindrical mirror for the reference pulse provides the same wavefront character as the scattered signal from the cylindrical target, and thereby removes any wavefront variation effects from the collection and focusing optics of the receiver [1], [2]. The reference pulse has a frequency bandwidth from 0.1 to 1.5 THz, as shown in Fig. 1(c),

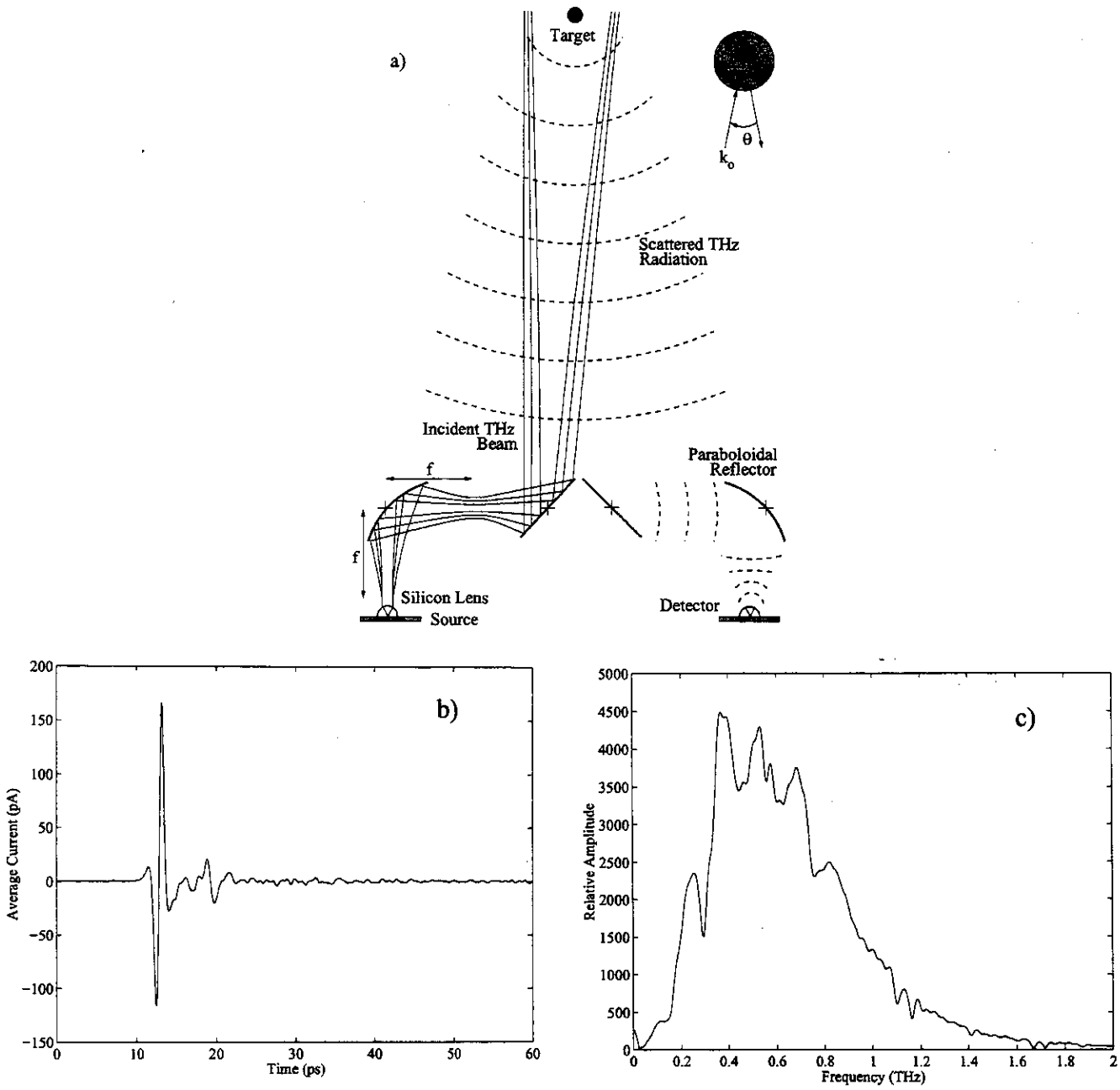

Fig. 1. (a) Terahertz impulse radar range. (b) Reference signal from a 30-mm-diameter metal cylinder. (c) Spectrum of the reference pulse.

and is polarized perpendicular to the axis of the cylinder. The experimental data, which is a four-scan average from the target cylinder, is shown in the upper plot of Fig. 2(a), where late time resonances are observed as far as 205 ps after the specular reflection labeled (S).

Using numerical analysis, the measured scattered field is compared with the exact solution for the infinitely long homogeneous cylinder [3]. The calculated complex spectrum of the scattered field at the detector is given by

$$E_{\text{scat}}(\theta,\omega) = E_{\text{ref}}(\omega)\frac{e^{ik_0 r}}{k_0 r}T_{\text{calc}}(\theta,\omega) \qquad (1)$$

where $k_0 = 2\pi/\lambda$ is the wave vector in free space, $T_{\text{calc}}(\theta,\omega)$ is the calculated complex scattering function for the target, and $E_{\text{ref}}(\omega)$ is the complex spectrum of the measured reference pulse. The scattered pulse in the time domain is obtained by taking the inverse fast-Fourier transform of $E_{\text{scat}}(\theta,\omega)$ and is shown in the middle plot of Fig. 2(a).

The accuracy of the terahertz range is demonstrated by the comparison of the experimental data and the theoretical calculation. When the data and theory are overlaid, the two graphs are virtually indistinguishable. Therefore, they are plotted separately in Fig. 2(a) by offsetting them. The arithmetical difference between the data and calculated theory is plotted as the lower curve to demonstrate the precision of the theoretical fit to the data. A direct comparison of the experimental data to the calculated fit is shown in Fig. 3, which is an enlargement of the feature labeled $\theta 1$ in Fig. 2(a).

For the same wavefront curvatures [1], [2], the ratio of the complex frequency spectra of the measured scattered electric

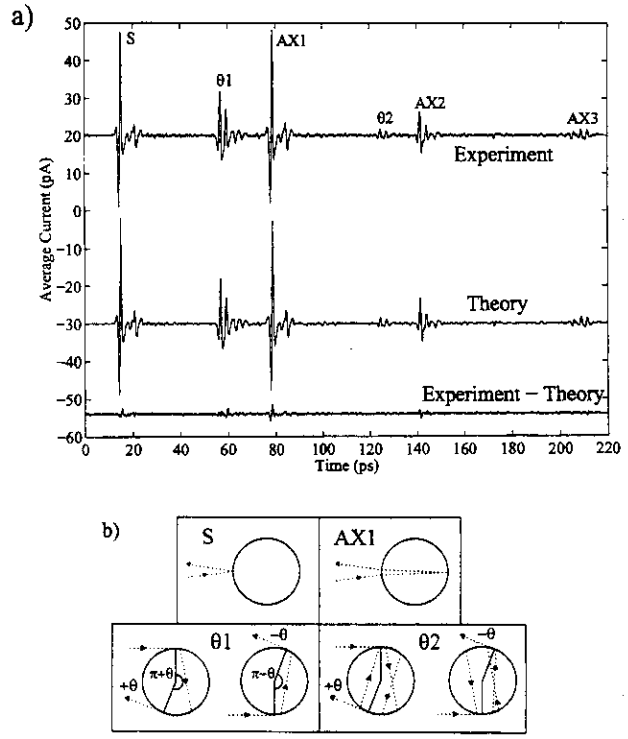

Fig. 2. (a) Scattering signature from a 3-mm-diameter alumina cylinder (upper) compared to the theoretically calculated signature (middle) and the difference between the two (lower). The identified scattering features are: S: specular reflection, $AX\#$: back axial reflection, and $\theta\#$: surface wave. (b) Diagrams of the three main scattering mechanisms.

field to that of the measured reference signal directly yields the measured complex scattering function of the target

$$T_{\text{meas}}(\theta, \omega, r) = E_{\text{meas}}(\omega)/E_{\text{ref}}(\omega). \tag{2}$$

From this, the frequency-dependent experimental RCS (σ_{RCS}) for a cylinder is calculated [1]–[3] as

$$\sigma_{\text{RCS}} = (4\pi/k_0 a)|T_{\text{meas}}(\theta, \omega, r)|^2. \tag{3}$$

The experimental value for the RCS is shown in Fig. 4 as points, which is compared to the theoretical RCS as the solid line. Due to the finite duration of the time-domain data, there is a windowing effect that limits the frequency resolution of the experimental RCS [4]. For a 220-ps temporal scan length, the corresponding full width at half maximum frequency resolution is 2.7 GHz. This limiting resolution is accounted for in the theoretical fit to the data shown in Fig. 4. Note the larger feature in the data at 1.16 THz; this is the position of a strong water absorption line, and the discrepancy with the calculated RCS is due to a slight reduction in the water vapor pressure between the time of the reference data scan and the dielectric cylinder data scan. This is due to a relative humidity difference of less than 0.5%.

To gain insight into the physical mechanisms involved in the scattering it is advantageous to apply the PO model [5] to the time-domain data since individual features are well resolved. Following this approach, three main scattering mechanisms can be distinguished: the first pulse labeled (S) in Fig. 2(a) is the specular reflection from the front surface of the cylinder, the next set of pulses labeled ($AX1$, $AX2$, $AX3$) are the multiple

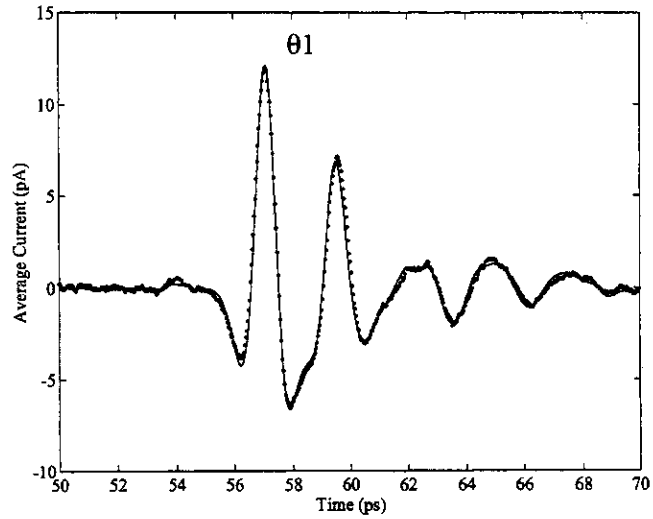

Fig. 3. First-order surface wave, $\theta 1$, experimental data (points) versus the numerical calculation (solid line).

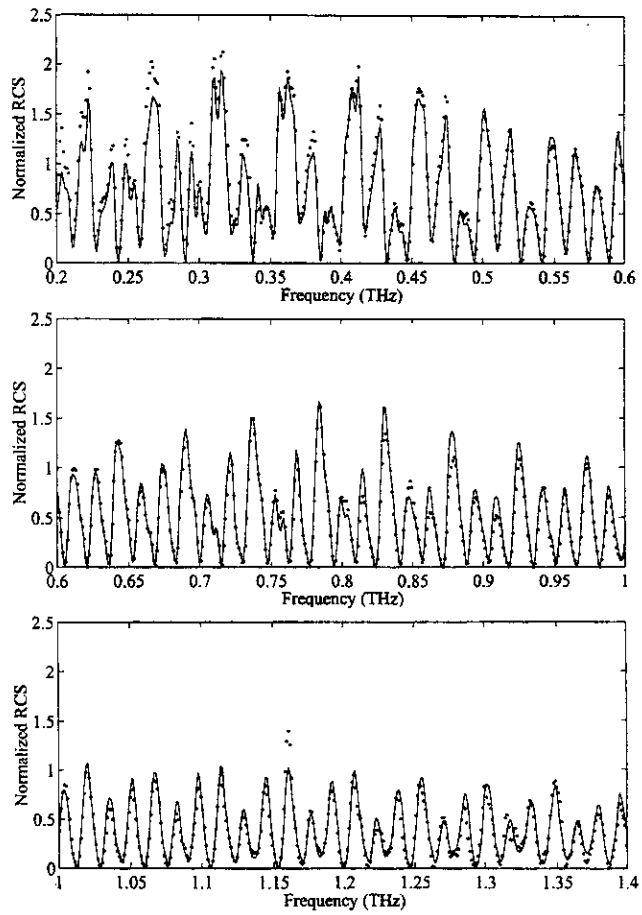

Fig. 4. Measured RCS (points) overlaid by the calculated RCS (solid line).

orders of reflections between the front and back surfaces of the target, and the third contributing type is the surface or creeping wave, of which we have successfully identified both the first-order $\theta 1$ and the second-order $\theta 2$. Schematic diagrams of all three classes are shown in Fig. 2(b). The small feature at 173 ps is from a small late time reflection in the reference pulse.

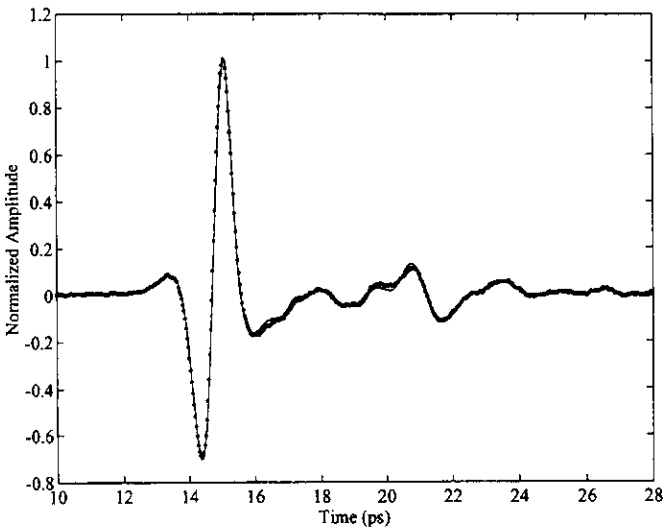

Fig. 5. Scaled and normalized overlay of the reference pulse (solid line) and the specular reflection (S) (points).

It is interesting to note that with the exception of signal size, the reference pulse of Fig. 1(b) and specular reflection (S) are essentially identical, as shown in Fig. 5, where the two pulses are normalized and overlaid. This remarkable similarity indicates that despite the order of magnitude difference in their diameters, both cylinders have the same flat frequency response; it also indicates that the receiver is clearly in the far field of the scatterings since a negligible difference is detected in the radius of curvature of their wavefronts. Also, the ratio of the reference pulse amplitude to that of the specular reflection from the dielectric cylinder is in excellent agreement with the expected value. For a cylinder, the amplitude of the reflection is expected to scale as the square root of the diameter, taking this into account as well as the reflection coefficient of 0.52 for the alumina, the expected amplitude difference is calculated to be 6.08, which is in excellent agreement with the experimental value of 6.11.

The impulse response signals S and $AX1$ have almost the same shape, but do not show the expected inversion of one to the other from their reflection coefficients having the opposite sign. The absent inversion is explained with the PO model when a phase correction term due to two single axis caustics is incorporated. The PO model is an extension of the geometrical optics approach to wave propagation. The phase accumulation in geometrical optics is not correct near a caustic (one axis focus), but if a $\pi/2$ phase shift is introduced for each single axis caustic the phase discrepancy is accounted for [6]. This relative phase accumulation for a beam that propagates through a focus is also known as the Gouy phase shift. In the case of the dielectric cylinder, the first back axial reflection ($AX1$) through the cylinder has two single axis caustics, one before and one after the back reflection. Therefore, for the PO model, an additional phase accumulation of π must be added to $AX1$ to account for these caustics, which, in turn, removes the relative inversion between S and $AX1$. It should also be noted that in scattering measurements of dielectric spheres a relative inversion does exist between S and $AX1$ [7]. In the case of a sphere, there is a two-axis caustic, as opposed to the single-axis caustic in the cylinder, before the back reflection, and a two-axis caustic after the reflection, yielding a total of 2π additional phase accumulation. This results in the relative phase inversion of S with respect to $AX1$ for the sphere, as one expects from the reflection coefficients.

As illustrated in Fig. 2(b), the surface wave is the result of coupling to the surface by the portion of the incident wave that is tangent to the cylinder. At some later point on the surface, the wave refracts through the cylinder at the critical angle α_c of the dielectric on a chord, which then couples back to the surface wave [5], [8]. It should be noted that the dual peak feature of $\theta 1$ and $\theta 2$ is due to detection at the bistatic angle θ of 13°. It follows that two surface waves are excited; one that propagates clockwise, $+\theta$, and the other counterclockwise, $-\theta$, as illustrated in Fig. 2(b). The wave $+\theta$ travels $\pi + \theta$ and $-\theta$ only $\pi - \theta$, therefore, $+\theta$ has traveled $2\theta a = 0.68$ mm further along the surface. Also, when comparing the first- and second-order surface waves, the second-order $\theta 2$ will have had each of its surface waves travel an additional 2π, consisting of two more chords, and the remainder traversed on the surface. Note that the temporal separation of the two features in $\theta 2$ is precisely the same as that of $\theta 1$, which is expected since each surface wave comprising $\theta 2$ has traveled an additional 2π; therefore, their relative delay remains unchanged.

Since the scattered signature of the first-order surface wave is temporally isolated, one can study its spectral content independent of the other late-time scattered features. By applying the PO model to the surface wave, important propagation characteristics can be determined. The optical path length of the two components of $\theta 1$ are completely defined by the cylinder-radius, the bistatic-angle, the frequency-dependent real part of the dielectric index of refraction $n_a(\omega)$, and an effective index of refraction of the surface wave (n_{eff}). Since both propagation directions travel through the same length chord, the difference in path length of the two waves is just the difference in their propagation lengths along the surface $D_{\pm\theta} = (\pi \pm \theta - 2\gamma) \cdot a$, where $\gamma = \pi/2 - \alpha_c$ is the interior half-angle subtended by the chord. The corresponding path lengths are 1.28 mm for $+\theta$ and 0.60 mm for $-\theta$. Likewise, the optical path length for each surface wave is $D_{\pm\theta} \cdot n_{\text{eff}}$. Therefore, from the time separation of 2.45 ps between the peaks of $\theta 1$, an estimate of the propagation velocity of the surface wave is found to be $0.92c$, which gives a real part of $n_{\text{eff}} = 1.08$; these values will be determined more precisely from the following frequency-domain analysis.

In the far field, the superposition of the $+\theta$ and $-\theta$ fields form the feature $\theta 1$. Using the reference pulse as the incident wave and following the PO model, the frequency-dependent complex amplitude is calculated with the following relation:

$$E_{\theta 1}(\theta, \omega) = A E_{\text{ref}}(\omega) \cdot e^{i(\pi/2)} \cdot \left[e^{i(2\pi a/\lambda) n_{\text{eff}} (\pi - 2\gamma)} e^{i(4\pi a/\lambda) n_a(\omega) \sin(\gamma)} \times \left(e^{i(2\pi a/\lambda)\theta n_{\text{eff}}} + e^{-i(2\pi a/\lambda)\theta n_{\text{eff}}} \right) \right]. \quad (4)$$

Here, n_{eff} and $n_a(\omega)$ are the complex indexes of refraction, which effect both phase and amplitude; A is a scaling parameter for $E_{\text{ref}}(\omega)$. The points in Fig. 6(a) are the numerical fast

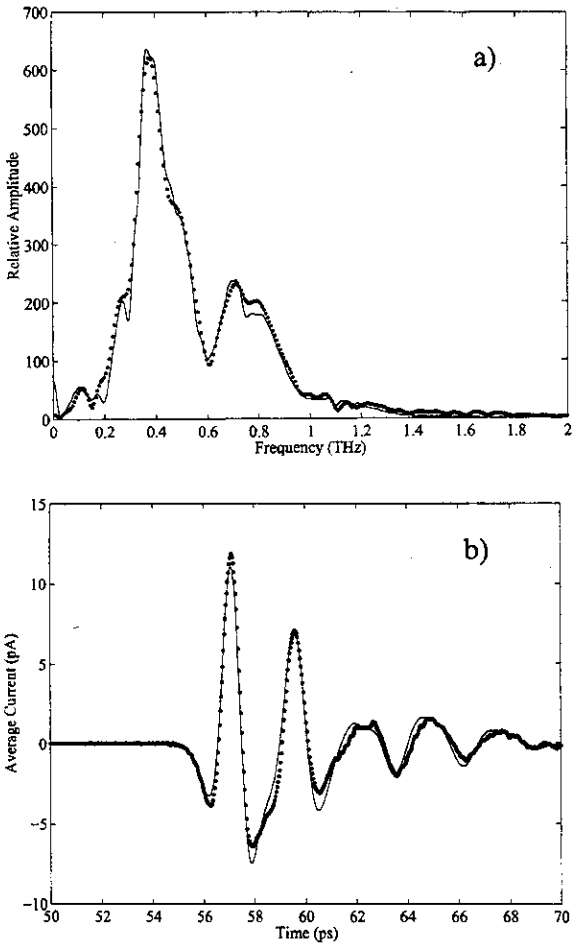

Fig. 6. (a) Spectrum of the first-order surface-wave $\theta 1$ (points) versus the numerically calculated fit based on the PO model with $n_{eff} = 1.10 + 0.073i$ (solid line). (b) Time-domain signal of calculated fit (solid line) versus data (points).

Fourier transform of $\theta 1$, as shown in Fig. 3, which has been temporally cut out of the entire pulse train. The solid line in Fig. 6(a) is a numerical fit using (4), where the only fitting parameters were the amplitude A, and the real and imaginary parts of n_{eff}. The real and imaginary parts of $n_a(\omega)$ have been determined by a separate measurement.[1] The phase term $e^{i\pi/2}$ in (4) is the phase correction term required because, in the case of the dielectric cylinder, the surface-wave chord through the cylinder has a single-axis caustic, thus, for the PO model, an additional phase accumulation of $\pi/2$ must be added. Of course, a phase change will not affect the frequency-domain fit of the surface wave, as shown in Fig. 6(a), but it has a pronounced effect on the inverse Fourier transform for the time-domain fit, as shown in Fig. 6(b).

The fit value for the effective index of refraction is $n_{\text{eff}} = 1.10 + 0.073i$. This value gives the surface wave velocity of $0.91c$. It should be noted that in the fit, a frequency-independent n_{eff} is used. Fig. 6(b) shows the measured time domain $\theta 1$ (points) and the corresponding time-domain PO fit (solid line) obtained by an inverse fast Fourier transform of the fit in Fig. 6(a). A previous experimental measurement of n_{eff} for the surface wave on a sphere has been performed on a 6.35-mm alumina sphere, where, with similar analysis, $n_{\text{eff}} = 0.98 + 0.08i$ was obtained, which yielded an effective velocity of c within the experimental error [7].

[1]Experimental measurements of the real and imaginary parts of the refractive index for alumina were fit with frequency-dependent mathematical equations. Writing the refractive index as $n_a(f) = n_r(f) + n_i(f)i$, the equations for the real and imaginary part are $n_r(f) = 3.17 + 0.0045f^2$ and $n_i(f) = 0.0024(f + 0.4f^2)$. Here f is the unitless magnitude of the frequency in terahertz, i.e., $f = 1$ at 1 THz. At 1 THz, the absorption is characterized by $n_i = 0.0033$ for alumina compared to 0.073 for the surface wave.

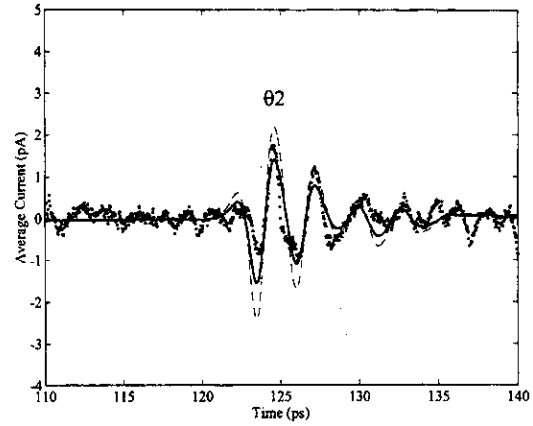

Fig. 7. Calculated second-order surface-wave $\theta 2$ based on n_{eff} derived from $\theta 1$. Dashed line: total coupling efficiency of 100%. Solid bold line: total coupling efficiency of 80%. Points: measured signal.

Having obtained a value for n_{eff} and knowing the complex frequency-dependent refractive index of alumina $n_a(\omega)$, the coupling efficiency from the surface wave to the chord and the reverse can be calculated since the data contains well-defined features for the first- and second-order surface waves. Both the $+\theta$ and $-\theta$ component of $\theta 2$ have propagated an additional revolution of the cylinder, as shown in Fig. 2(b); the total optical path length $\Delta D(\omega)$ consists of the two additional chords as well as surface-wave propagation, and is given by $\Delta D(\omega) = an_a(\omega) \cdot (4 \sin \gamma) + an_{\text{eff}}(2\pi - 4\gamma)$. The additional surface-wave propagation for the two components of $\theta 2$ is 1.88 mm. The frequency-dependent electric field of $\theta 2$ is

$$E_{\theta 2}(\theta, \omega) = E_{\theta 1}(\theta, \omega) \cdot (C_{12}C_{21})^2 \cdot e^{i\pi} \cdot e^{ik_0 \Delta D(\omega)} \quad (5)$$

where $E_{\theta 1}(\theta, \omega)$ is either given by (4) or, for the calculation to follow, is the complex spectrum of the experimentally measured $\theta 1$. $C_{12}C_{21}$ is the total coupling efficiency through the dielectric medium, where C_{12} is the field coupling into the dielectric and C_{21} is the coupling out of the dielectric. The total coupling through the two surfaces, i.e., $C_{12}C_{21}$, is squared since the surface wave will have traversed two more chords in the additional 2π propagation of $\theta 2$. It should be noted that there is also a factor of $C_{12}C_{21}$ contained in the scaling factor A of (4), but its value is intractable due to the required scaling of the reference pulse. The extra phase factor of $e^{i\pi}$ is from the two single-axis caustics in the two additional chords of propagation. Performing a numerical inverse fast Fourier transform on $E_{\theta 2}(\theta, \omega)$, the time-domain pulse is obtained and plotted versus the data (points) for $\theta 2$ in Fig. 7. The dashed line in Fig. 7 is the calculated $\theta 2$ assuming a coupling efficiency of $C_{12}C_{21} = 1$. The comparison of the size of $\theta 2$ (with $C_{12}C_{21} = 1$) with respect to $\theta 1$ [see Fig. 2(a)] shows that most of the signal reduction

of $\theta 2$ is accounted for by the propagation effects of the wave on the surface and to a minor extent through the alumina. Compared to $\theta 1$, the $+\theta$ and $-\theta$ components of $\theta 2$ traverse an additional 1.88 mm on the surface and 5.68 mm through the alumina. Most of the attenuation is due to the much larger loss of the surface wave compared to that of alumina, even though the path through alumina is three times longer. The surface-wave loss is due to radiation leakage, while in the alumina power is absorbed. To obtain the coupling efficiency, the dashed line is multiplied by $(C_{12}C_{21})^2$ for the best fit to the data and plotted as the bold solid line in Fig. 7, yielding a total coupling efficiency of $C_{12}C_{21} = 0.8 \pm 0.1$, where the uncertainty was obtained through least-squares-fit methods. Although it is a crucial parameter for the PO model, the surface-wave coupling efficiency has not been previously measured.

III. Conclusion

Through a time-domain measurement of a 3-mm-diameter alumina cylinder as a target, we have demonstrated the precision of our time-domain terahertz-impulse radar range. Previously, this range has been used to perform introductory experiments on 1:200-scale model targets [1], [2]. The added accuracy that has now been demonstrated allows the extension of these measurements to more complex targets. The accuracy of the PO model when applied to scattering has been verified. However, we have experimentally shown that, in the time domain, it is essential that all phase terms are included, in particular, the Gouy phase, which is the accumulated phase acquired when propagating through a caustic or focus. From the experimental measurement, a total surface-wave coupling efficiency through the cylinder of 80% was obtained and the effective index of refraction was found to be $1.10 + 0.073i$, yielding a propagation velocity of $0.91c$.

References

[1] R. A. Cheville and D. Grischkowsky, "Time domain terahertz impulse ranging studies," *Appl. Phys. Lett.*, vol. 67, pp. 1960–1962, 1995.

[2] R. A. Cheville, R. W. McGowan, and D. Grischkowsky, "Late-time target response measured with terahertz impulse ranging," *IEEE Trans. Antennas Propagat.*, vol. 45, pp. 1528–1524, Oct. 1997.

[3] D. E. Barrick, *Radar Cross Section Handbook*, G. T. Ruck, Ed. New York: Plenum, 1970, vol. 1.

[4] R. A. Cheville and D. Grischkowsky, "Foreign and self broadened rotational linewidths of high temperature water vapor," *J. Opt. Soc. Amer. B, Opt. Phys.*, vol. 16, pp. 317–322, Feb. 1999.

[5] J. Rheinstein, "Backscatter from spheres: A short pulse view," *IEEE Trans. Antennas Propagat.*, vol. AP-16, pp. 89–97, Jan. 1968.

[6] R. G. Kouyoumjian, L. Peters, Jr., and D. T. Thomas, "A modified geometrical optics method for scattering by dielectric bodies," *IEEE Trans. Antennas Propagat.*, vol. AP-11, pp. 690–703, Nov. 1963.

[7] R. A. Cheville, R. W. McGowan, and D. Grischkowsky, "Time resolved measurements which isolate the mechanisms responsible for terahertz glory scattering from dielectric spheres," *Phys. Rev. Lett.*, vol. 80, pp. 269–272, 1998.

[8] H. Inada, "Backscattering short pulse response of surface waves from dielectric spheres," *Appl. Opt.*, vol. 13, pp. 1928–1933, 1974.

Roger W. McGowan was born in Saint Paul, MN, on July 7, 1966. He received the B.A. degree in physics from Gustavus Adolphus College, St. Peter, MN, in 1988, and the Ph.D. degree in physics from Colorado State University, Fort Collins, in 1996. His thesis research concerned the light forces on atoms, where he demonstrated that there is a viable atomic transition in aluminum atoms suitable for light-force manipulation of atoms. This research led to his dissertation on "Light force cooling, manipulation, and nanometer-scale deposition of neutral aluminum atoms."

He is currently a Visiting Assistant Professor with the Multidisciplinary Center for Laser and Photonic Research, Oklahoma State University, Stillwater. His current research interests are ultrafast optoelectronics, generation and applications of terahertz radiation, and ultrashort electrical pulse propagation on micro-transmission lines and broad-band terahertz waveguides.

Dr. McGowan is a member of the Optical Society of America and the American Physical Society.

R. Alan Cheville received the BSEE and Ph.D. degrees from Rice University, Houston, TX, in 1986 and 1994, respectively.

He is currently an Assistant Professor in the Department of Electrical and Computer Engineering, Oklahoma State University, Stillwater. His research interests have included electron-beam-pumped tunable excimer lasers, broadly tunable second harmonic generation systems for short pulse lasers, and ultrafast time-resolved spectroscopy. His research interests are focused on applications of optoelectronically generated terahertz radiation and high-speed optoelectronics.

Dr. Cheville is a member of the American Physical Society and the Optical Society of America.

Daniel R. Grischkowsky (A'84–SM'90–F'92) was born in St. Helens, OR, on April 17, 1940. He received the B.S. degree from Oregon State University, Corvallis, in 1962, and the Ph.D degree in physics from Columbia University, New York, NY, in 1968. His thesis work involved electron spin resonance investigations and led to the explanation of the magnetic-field dependence of photon echoes in ruby.

In 1969, he joined the Watson Research Center, IBM, Yorktown Heights, NY. His initial experimental and theoretical research involved studying the interaction between near-resonant light and the two-level system. The adiabatic following model, which he originally proposed as a result of these studies, explained the observed effects of self-focusing, self-defocusing, self-steepening, and slow group velocities in vapors of alkali metals. His subsequent experimental and theoretical studies of the nonlinear propagation of picosecond laser pulses in single-mode optical fibers led to the invention of the optical-fiber pulse compressor and to the experimental observations of gray solitons and optical intensity shocks. He has since shifted his studies to ultrafast optoelectronics, initially focusing on the generation and applications of subpicosecond electrical pulses on transmission lines. An important part of this work has been the observation terahertz radiation from the generation site and Cherenkov radiation from the propagating electrical pulses. These studies have resulted in new sources of pulsed terahertz beams, which have enabled the new technique of terahertz–time-domain spectroscopy (THz–TDS). In 1993, he joined Oklahoma State University, Stillwater, as the Bellmon Professor of optoelectronics in the School of Electrical and Computer Engineering. At Oklahoma State University, his work has concentrated on unique applications of THz–TDS, including determining the nature of conductivity in semiconductors, terahertz (far-infrared) characterizations of flames, and terahertz impulse scale ranging.

Dr. Grischkowsky is a Fellow of the Optical Society of America and the American Physical Society. He was awarded the 1985 Boris Pregel Award for Applied Science and Technology presented by the New York Academy of Sciences for his invention of the optical-fiber pulse compressor. He also received the 1989 R. W. Wood Prize presented by the Optical Society of America for his pulse propagation studies in optical fibers and their use for generating ultrashort pulses of light.